What controls the along-strike slopes of volcanic rift zones?

Yuri A. Fialko[1] and Allan M. Rubin

Department of Geosciences, Princeton University, Princeton, New Jersey

Abstract. We investigate the dynamics of viscous pressure losses associated with lateral magma transport in volcanic rift zones by performing (1) coupled elastic-hydrodynamic simulations of downrift magma flow in dikes and (2) analog experiments mimicking lateral dike propagation in the presence of an along-rift topographic slope. It is found that near-source eruptions are likely to be favored by shallow slopes while distant downrift eruptions may be encouraged by steeper slopes, provided that along-rift variations in the tectonic stress are negligible or uncorrelated on the timescale of multiple dike intrusions. This implies the existence of a critical slope to which a volcanic rift zone would naturally evolve. Such behavior is produced by three-dimensional (3-D) elastic effects and is controlled by the ratio of the driving pressure gradient due to the along-strike topographic slope to the vertical gradient in the excess magma pressure in the dike. This model may be viewed as complementary to commonly cited mechanisms that appeal to magma viscosity and the dynamics of freezing of lava flows at the surface to explain the low profiles of basaltic shield volcanoes. Our estimated values of the critical slopes are in general agreement with observations in Hawaiian rift zones, but further development of fully 3-D models is required for more accurate predictions.

1. Introduction

Volcanic rift zones are regions where new crust is formed as a result of interaction between mafic volcanism and extensional tectonics. The morphology of volcanic rift zones varies greatly between different settings on Earth, as well as between Earth and other terrestrial planets. Nonetheless, rift zones extending from discrete magmatic centers are almost universally characterized by the presence of along-strike topographic slopes. These slopes are generally of the order of a few percent and tend to be fairly uniform along strike (Figure 1). In many cases (e.g., Hawaii), they are also considerably shallower than across-strike slopes. The nature of these variations in surface elevation is not well known. While it is generally recognized that the observed topography is produced by some combination of volcanic construction, fault tectonics, mass wasting, and (for subaerial volcanic rift zones on Earth) erosion, the particular mechanisms involved are still poorly understood. For instance, the gentle slopes of shield volcanoes are commonly attributed to the low viscosity and/or high effusion rates of the erupted basaltic lavas [e.g., *MacDonald et al.*, 1983; *Mark and Moore*, 1987]. That is, low-viscosity lavas travel large distances from the eruption site before freezing, which effectively spreads the erupted volume over a large area. However, it seems that the dynamics of lava cooling by itself cannot be invoked to explain the systematics of the along-strike topography of volcanic rift zones. This is because magma that reaches the surface during individual fissure eruptions flows nearly perpendicular to the rift zone axis, following the steeper across-strike slopes, i.e., in the wrong direction if it were to control the along-rift topography. This is vividly demonstrated by the shape of lava flows erupted along the currently active volcanic rift zones of Mauna Loa and Kilauea in Hawaii [e.g., *Holcomb*, 1987]. *Dieterich* [1988] has suggested that the across-strike slopes of volcano flanks may be governed by the balance between friction on the basal decollement faults and a hydrostatic push due to the intruded magma. While this mechanism may be relevant to the across-rift topography, it also fails to address the origins of the along-rift slopes.

In this paper we investigate one possible mechanism by which the observed along-strike topographic slopes could result from the dynamics of the shallow "plumbing" system of the rift. Field studies indicate that volcanic rift zones are composed of extensive dike swarms transporting magma downrift from a central magma chamber [*Fiske and Jackson*, 1972; *Pollard et al.*, 1983; *Knight and Walker*, 1988]. Therefore it is reasonable to assume that the long-term along-strike topography of volcanic rift zones is to a large extent controlled by eruptive patterns of laterally propagating dikes and thus in some average sense reflects viscous pressure losses within these dikes. To simplify the problem and gain some general insight into the fluid-mechanical aspects of dike emplacement, we consider models of dike propagation in the limit of negligible along-rift variation in the tectonic stress. The assumption of uniform tectonic stresses may be appropriate, for example, during volcanically robust shield-building phases when magmatic input periodically imposes a lithostatic state of stress everywhere along the rift. In the presence of substantial along-strike variations in the tectonic

[1] Now at Seismological Laboratory, California Institute of Technology, Pasadena.
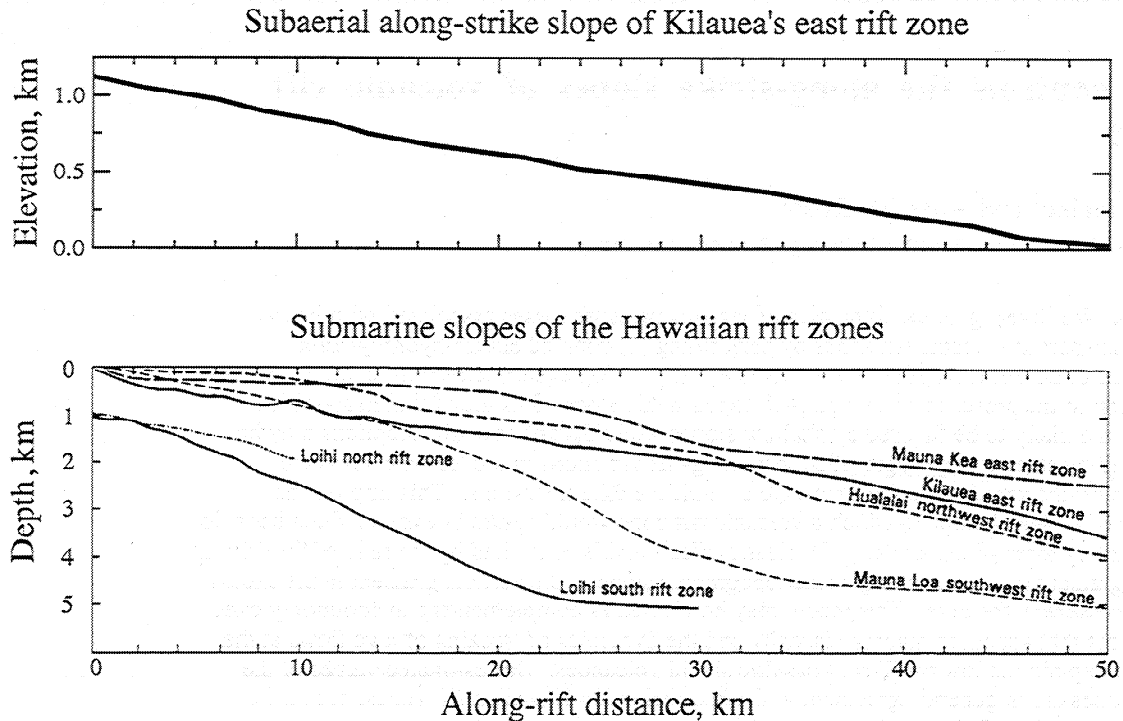
Figure 1. Along-strike slopes of volcanic rift zones in Hawaii. Data are taken from *Holcomb* [1987] and *Fornari* [1987].

stresses (a likely case, e.g., on slow spreading mid-ocean ridges) the situation is more complex. First, along-strike variations in the horizontal stress may affect volcanic construction by dictating the position of eruption sites. Second, nonuniform extension may result in different degrees of normal faulting and crustal thinning along the rift which may affect topography either directly or via isostatic adjustment. The effects of tectonic loads may in principle be incorporated in the model discussed below if the along-strike variations in crustal stresses are known a priori. Unfortunately, this is rarely the case. While recognizing that lateral stress variations may be important in some instances, we shall demonstrate that the values and constancy of the along-strike slopes of volcanic rift zones may be explained by dynamic aspects of magma transport in a homogeneously stressed medium. Note that the effects of nonuniform tectonic stresses that result from periodic dike intrusions might

"average out" on the timescale of several generations of intrusions. For simplicity, we shall also neglect thermal effects (e.g., temperature-dependent magma viscosity, freezing, etc.). Implications of these assumptions for our results are discussed further in section 6. We begin by considering the emplacement of a single dike propagating in the presence of a small along-rift topographic slope (Figure 2).

2. Driving Forces and Governing Equations

As established by field observations and theoretical and physical modeling [*Fiske and Jackson*, 1972; *Rubin and Pollard*, 1987; *Ryan*, 1987; *Lister and Kerr*, 1991], lateral dikes propagate along the level of neutral buoyancy (LNB) that physically corresponds to the depth at which the vertical gradient in the excess magma pressure changes sign [*Fialko and Rubin*, 1998]. For simplicity, we assume that the LNB
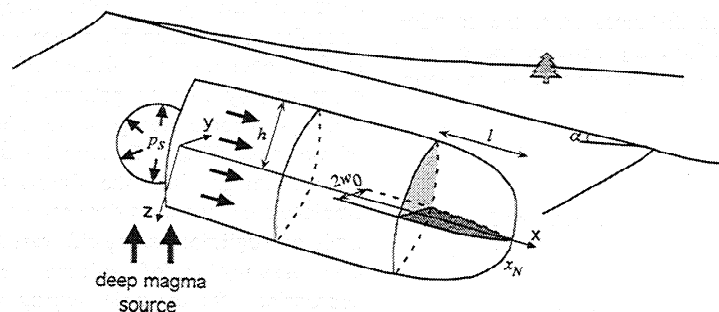

Figure 2. A dike propagating along the level of neutral buoyancy (LNB) in the presence of a small topographic slope α. The flow is fed by a source (e.g., shallow magma chamber) at constant pressure p_s.

parallels the Earth's surface and that the dike is symmetric with respect to the LNB (should these conditions be relaxed, the following analysis would be applicable with simple modifications of the governing parameters). Magma is supplied at the source having a constant pressure p_s and is driven by variations in the excess magma pressure along the dike $\partial p / \partial x$ and by the driving pressure gradient due to gravity

$$G = \rho_d g \sin \alpha, \qquad (1)$$

where α is the along-strike topographic slope, g is the gravitational acceleration, and ρ_d is the density difference between the magma and air or water in the case of subaerial or submarine rift zones, respectively. For most rift zones the along-strike slope is small (of the order of 1-10%), and $\sin \alpha \approx \alpha$. For excess magma pressures of several megapascals (consistent with observations of dike widths of a few meters) and characteristic along-strike slopes of the rift zones of several percent [e.g., *Fiske and Jackson*, 1972; *Rubin and Pollard*, 1987], dikes need to be longer than $p_s/G \sim 10$ km in order to be driven essentially by the topography [*Fialko and Rubin*, 1998]. For volcanic rift zones having lateral extents of order of 10^2 km (e.g., in Hawaii) [*Fornari*, 1987], it is probable that the bulk of the downrift melt transport there is topography-driven.

Assuming that the magma flow is one-dimensional, laminar, and Newtonian, local conservation of mass is given by

$$\frac{\partial w}{\partial t} = \frac{1}{3\eta} \frac{\partial}{\partial x} \left[w^3 \left(\frac{\partial p}{\partial x} - G \right) \right], \qquad (2)$$

where w is the dike half width and η is the magma dynamic viscosity. Equation (2) states that the rate of dike opening at a particular point is produced by a local divergence of volume flux. The excess magma pressure p opening the dike is given by the difference between the magma pressure and the ambient normal stress. As mentioned in section 1, we are interested in the case when the along-dike variations in the ambient normal stress are small compared with either the excess pressure at the source or G. In our analysis we assume that the energy required to fracture the host rock is negligible compared with viscous dissipation in the magma [*Stevenson*, 1982; *Lister and Kerr*, 1991]. The implications of relaxing this assumption are considered in section 6; essentially, if the fracture energy is sufficient to impede the flow, then in the presence of a topographic slope downrift eruptions are favored.

For dikes having lateral extent x_N substantially exceeding the dike height $2h$ (Figure 2), the dike thickness profile in any vertical cross section far from the leading edge depends on the excess pressure distribution in that section alone. This is because along-strike variations in excess pressure are small and the deformation is well approximated by plane strain conditions. Following *Lister* [1990] and *Lister and Kerr* [1991], we consider two canonical distributions of the dike-perpendicular stress with depth capable of trapping dikes at the level of neutral buoyancy. In the first case, corresponding to a density step between the two layers of rock, the excess magma pressure distribution $p(z)$ varies piecewise linearly with depth with a kink at the LNB $z = 0$. That is, $p(z) = p_0 - \Delta\rho gz$, where p_0 is the excess pressure at the depth of the dike middle and $\Delta\rho$ is the density contrast between the magma and the host rocks that is negative above the LNB and positive below. By imposing the condition of zero stress intensity factors at the dike top and bottom (see equation (A3) in the appendix), one

obtains the following relation between p_0 and the dike half height h:

$$p_0 = \frac{2}{\pi} \Delta\rho gh. \qquad (3)$$

In the second case, the rock density increases linearly with depth and the excess magma pressure distribution is parabolic,

$$p(z) = p_0 + (\rho_m - \rho_0)z - \frac{R}{2} z^2,$$

where ρ_m is the magma density, ρ_0 is the host rock density at the LNB, and R is the host rock density gradient. We consider the case $\rho_0 = \rho_m$, which gives rise to symmetry with respect to the LNB. The requirement of zero stress intensity factors at the dike edges in this case gives rise to the relation

$$p_0 = \frac{1}{4} Rgh^2. \qquad (4)$$

The maximum dike half width w_0 may be related to the dike half height h using two-dimensional (2-D) elastic solutions for equilibrium cracks in an infinite body [*Lister*, 1990; *Khazan and Fialko*, 1995],

$$w_0 = \varphi \frac{p_0}{M} h, \qquad (5)$$

where M is the elastic stiffness of the host rocks, $M = \mu/(1-\nu)$, μ being the shear modulus and ν being Poisson's ratio. The dimensionless coefficient φ depends on the excess pressure distribution with depth and specified fracture criterion. For a uniform excess pressure distribution resulting in stress intensity factors $p_0 h^{1/2}$ at the dike edges, $\varphi = 1$. Assuming zero stress intensity factors at the dike tips, one obtains $\varphi = 1/2$ for the piecewise linearly varying excess pressure (density step LNB) and $\varphi = 2/3$ for the quadratically varying excess pressure (density gradient LNB) (see, e.g., *Lister* [1990] for details).

Because under plain strain conditions the dike width, height, and excess magma pressure are related through 2-D elasticity and may be expressed as simple functions of each other, equation (2) may be integrated over the dike height to yield a cross-sectionally averaged continuity equation in terms of one unknown (e.g., the dike height) only. For a dike propagating along a density step LNB, we obtain

$$\frac{\partial h^3}{\partial t} = \frac{2\varpi}{3\eta M^2} \left(\frac{\Delta\rho g}{\pi} \right)^3 \frac{\partial}{\partial x} \left[h^7 \left(\frac{\partial h}{\partial x} - \gamma \right) \right], \qquad (6)$$

where $\gamma = \pi G / 2\Delta\rho g$ is essentially a ratio of the driving pressure gradient due to topography to the vertical gradient in the excess magma pressure, and ϖ may be interpreted as a dimensionless cross-sectionally averaged magma velocity given by

$$\varpi = \frac{\int_0^1 W^3 d\bar{z}}{\int_0^1 W d\bar{z}}, \qquad (7)$$

where $\bar{z} = z/h(x,t)$ and $W(\bar{z}) = w(z)/w_0$ (for given x) is a self-similar crack profile [*Lister*, 1990]. For a symmetric 2-D crack with a linearly varying excess pressure, $\varpi \approx 0.6$. Nondimensionalization of (6) with respect to the scales

$$\hat{h} = h_s, \quad \hat{x} = h_s, \quad \hat{t} = \frac{3\eta M^2}{2\varpi} \left(\frac{\pi}{\Delta\rho gh_s} \right)^3, \qquad (8)$$

where h_s is the dike half height at the source ($x = 0$), gives rise to the following second-order nonlinear partial differential equation for the dimensionless dike height $\bar{h} = h/\hat{h}$:

$$\frac{\partial \bar{h}}{\partial \bar{t}} = \frac{\bar{h}^4}{3}\left[\bar{h}\frac{\partial^2 \bar{h}}{\partial \bar{x}^2} + 7\frac{\partial \bar{h}}{\partial \bar{x}}\left(\frac{\partial \bar{h}}{\partial \bar{x}} - \gamma\right)\right], \qquad (9)$$

where $\bar{x} = x/\hat{x}$, $\bar{t} = t/\hat{t}$, and it is assumed that γ is independent of x. On the assumption that the 2-D approximation is valid all the way to the leading edge of the dike (a point to which we shall return below), equation (9) may be solved numerically given some initial height distribution, subject to the boundary conditions $\bar{h} = 1$ at the source ($\bar{x} = 0$) and $\bar{h} = 0$ at the leading edge ($\bar{x} = \bar{x}_N$). For $\gamma = 0$ (i.e., in the absence of a topographic driving pressure gradient), *Lister* [1990] obtained a family of elegant self-similar solutions to (9) in which the dike volume V was specified to vary as a power law function of time, $V \propto t^a$, where a is a numerical constant. The dike height profile for the geologically interesting case of constant source pressure (which follows from Lister's general solution for $a = 0.5$) is shown in Figure 3a. As illustrated by Figure 3a, the height, width, and excess pressure of a dike driven by an excess source

pressure all monotonically decrease toward the leading edge, reflecting the viscous pressure losses associated with dike advance. Such dikes would be most likely to erupt directly above the source, i.e., where their height is greatest.

When $\gamma \neq 0$ (in the presence of an external driving pressure gradient), self-similarity does not hold, and equation (9) must be integrated from given initial conditions. However, one may observe that for $\gamma \gg |\partial \bar{h}/\partial \bar{x}|$ (i.e., when the dike "tail" is long enough that the dominant driving pressure gradient for the flow is provided by the topography), equation (9) has a trivial solution for the dike tail, $\bar{h} = \text{const} = 1$. Constant height in the dike tail, together with the constant driving pressure gradient provided by the topographic slope, implies constant magma flux through the tail. This suggests that the "nose" of a sufficiently long dike may propagate in a steady state fashion at the dimensionless velocity $\partial \bar{x}_N/\partial \bar{t} = \gamma$ dictated by the flux from the tail while preserving its shape in the reference frame of the advancing magma front. Provided the assumption of steady state (or sufficiently slowly varying) conditions within the nose is valid, we introduce a moving reference frame with along-flow coordinate $\xi = \bar{x} - \bar{x}_N(\bar{t})$ and put $\partial \bar{h}/\partial \bar{t} = 0$ to obtain from (9)

$$\frac{1}{3}\bar{h}^5\bar{h}'' + \frac{7}{3}\bar{h}^4\bar{h}'^2 - \gamma\bar{h}'\left(\frac{7}{3}\bar{h}^4 - 1\right) = 0, \qquad (10)$$

where $\bar{h}' = d\bar{h}/d\xi$. Integration of (10) with appropriate boundary conditions $\bar{h} = 0$ for $\bar{h} = 1$ and $\bar{h} = 0$ for $\xi = 0$ yields

$$\bar{h} - \frac{1}{2}\arctan \bar{h} + \frac{1}{4}\ln\left|\frac{1-\bar{h}}{1+\bar{h}}\right| = \gamma\xi. \qquad (11)$$

The dimensionless dike height $\bar{h}$ over the dike nose is shown in Figure 3b as a function of the scaled dimensionless distance behind the dike leading edge. As may be seen from Figure 3b, (11) predicts a nose length (dimensionally) of the order of γh_s, over which the dike height monotonically decreases from its constant value in the tail to zero at the leading edge.

Comparison of Figures 3a and 3b indicates that for a given topographic slope, dikes that are shorter than p_s/G are most likely to erupt near the source and thus tend to increase the along-strike slope of volcanic rift zone, while much longer dikes may erupt essentially anywhere along their propagation path. Equation (11) predicts that topography-driven dikes would passively track a given slope without the ability to systematically modify the latter. However, the leading edges of actual dikes do not look like the ones shown in Figure 3. As is demonstrated below, by neglecting the intrinsic three-dimensionality of elastic displacements in the dike nose region we have omitted some important dynamic aspects of magma flow which may cause dikes to increase their height downrift, given sufficiently large slopes. The possibility of such behavior may be rationalized from the following qualitative argument. Within the dike nose, decreases in elastic thickness near the leading edge must be offset by increases in the magma pressure gradient in order to maintain the constant propagation velocity of a topography-driven dike. Dimensionally, the magnitude of the available additional driving pressure gradient is of the order of p_s/l, where l is an effective nose length (Figure 2). Because the nose length l cannot be substantially smaller than the dike height due to the constraints of 3-D elasticity, for sufficiently large topographic
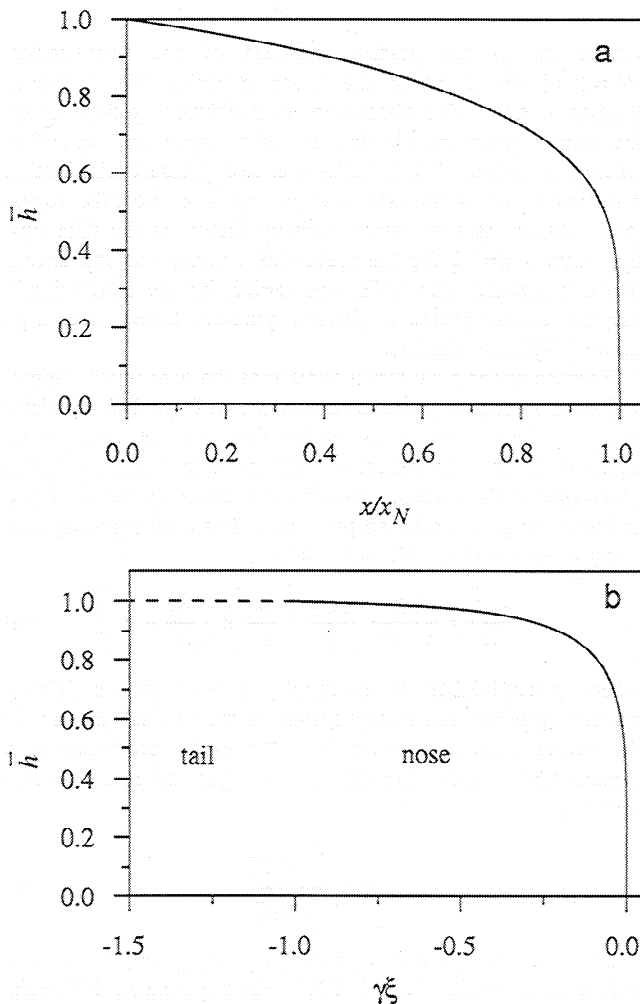

Figure 3. (a) Self-similar dike height for a dike trapped at a density step LNB and driven by the excess source pressure (equation (9)). (b) Height near the leading edge of a steady state topography-driven dike (equation (11)).

slopes (e.g., when $G > p_s/l$), the excess pressure gradient in the nose may not be able to drive the magma through the narrowing nose at the velocity dictated by the incoming flux from the dike tail. As a result, the nose will act as a "bottleneck" restraining the flow, so the dike must respond by "inflating" the nose (i.e., by increasing the excess magma pressure some distance behind the leading edge), which increases the nose thickness and the velocity at which magma flows through it. In principle, this increase in excess magma pressure may result in local increases in the nose height. This would, in turn, favor downrift eruptions and in the long term could tend to reduce the along-strike slope. To gain further quantitative insight into the dynamics of viscous pressure losses in such a dike, we consider a simplified model in which vertical and horizontal 2-D solutions are matched at the base of the dike nose and variations in the dike thickness and excess pressure in the vertical direction are neglected.

3. Matched Two-Dimensional Solutions

Sufficiently close to the dike leading edge (i.e., closer than the local dike half height), plane strain conditions are more likely to be satisfied in a horizontal than a vertical cross section through the dike. We analyze magma flow in the median (horizontal) cross section through the dike (the plane $z = 0$ in Figure 2) near the dike leading edge using a coupled elastic-hydrodynamic model for a 2-D fluid-driven crack described in the appendix. On the basis of the above argument for a topography-driven dike, the crack is assumed to have a steady state shape and to move at a constant velocity u_{nose},

$$u_{nose} = -\frac{w^2}{3\eta}\left(\frac{\partial p}{\partial x} - G\right) = \frac{p_n^3 l}{3\eta M^2}U(\Gamma), \qquad (12)$$

where w and p are the nose half thickness and the magma excess pressure in the plane $z = 0$, respectively, p_n is the excess pressure at the base of the nose, $\Gamma = Gl/p_n$ is essentially the ratio of the driving pressure gradients due to topography and excess magma pressure, and $U(\Gamma)$ is a dimensionless nose velocity to be found from the corresponding boundary value problem (see the appendix). In a dike tail having a half width w_0 (Figure 2) the average magma velocity in the median cross section u_{tail} is given by

$$u_{tail} = \frac{w_0^2 G}{3\eta}. \qquad (13)$$

The assumption of steady state propagation implies that

$$u_{nose} = u_{tail}. \qquad (14)$$

Making use of an a priori statement that the nose length l be proportional to the dike half height h,

$$l = \lambda h, \qquad (15)$$

where the proportionality coefficient $\lambda \sim O(1)$, from (5) and (12)-(15) one can obtain a simple expression for the ratio of the excess pressure at the base of the dike nose to the excess pressure back in the dike tail,

$$\frac{p_n}{p_0} = \frac{\varphi}{\lambda}\left(\frac{\Gamma}{U(\Gamma)}\right)^{1/2}, \qquad (16)$$

where the constant φ is defined in (5). The dimensionless nose velocity U is a function of two parameters, the dimensionless topographic driving pressure gradient Γ and a dimensionless tip suction P_t (see the appendix for details). Solutions for $U(\Gamma;P_t)$ are shown in Figure 4. As one might expect, U depends rather weakly on the tip suction [e.g., *Rubin*, 1993], so without loss of generality the latter may be excluded from the list of independent parameters. We use $P_t = -2$ in our further calculations. Also, as is evident from Figure 4, for Γ larger than unity, U depends on Γ almost linearly. This result is expected as well given that for Poiseuille flow the velocity scales linearly with the driving pressure gradient.

It is instructive to consider an asymptotic solution for large values of Γ. In this case, (16) reduces to

$$\frac{p_n}{p_0} = k^{-1/2}\frac{\varphi}{\lambda}, \qquad (17)$$

where k is the slope of the $U(\Gamma)$ curve for large Γ. Figure 5 shows the range of dimensionless thicknesses of the dike tail φ and dimensionless nose lengths λ at which the excess magma pressure at the base of the dike nose is predicted to exceed that in the dike tail. As follows from (17) and Figure 5, increasing φ encourages buildup of pressure in the dike nose. This implies, in particular, that the density step LNB would be the least effective among geologically reasonable excess pressure distributions with depth ("concave," i.e., such that $\partial^2 p/\partial z^2 > 0$) in producing increases in the excess pressure at the base of the nose.

Note that while φ is given by 2-D solutions for the dike tail, λ (or the dimensional nose length l) is yet to be defined in a self-consistent fashion. One way of constraining λ is to require that the dike opening at the base of the nose (computed using a 2-D horizontal cross section) equals that in the dike tail (computed using a 2-D vertical cross section and given by equation (5)),

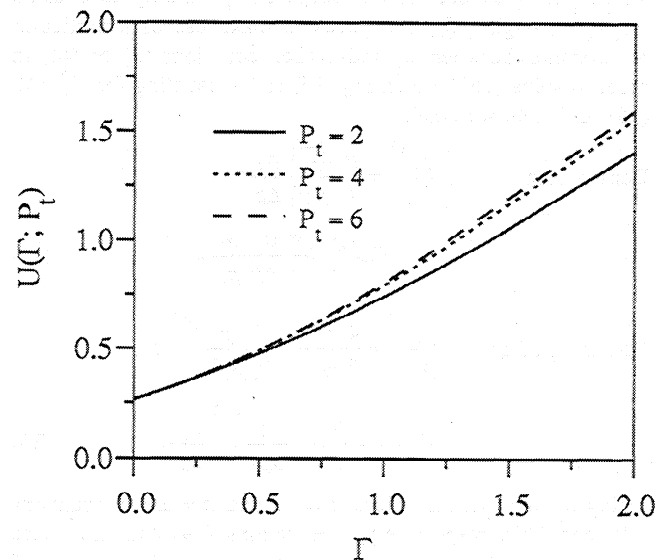$$\omega(0)\frac{p_n}{M}l = w_n = \varphi\frac{p_n}{M}h, \qquad (18)$$

Figure 4. Nondimensional velocity of a two-dimensional (2-D) crack as a function of the dimensionless driving pressure gradient due to topography $\Gamma = Gl/p_n$ (see main text and appendix).
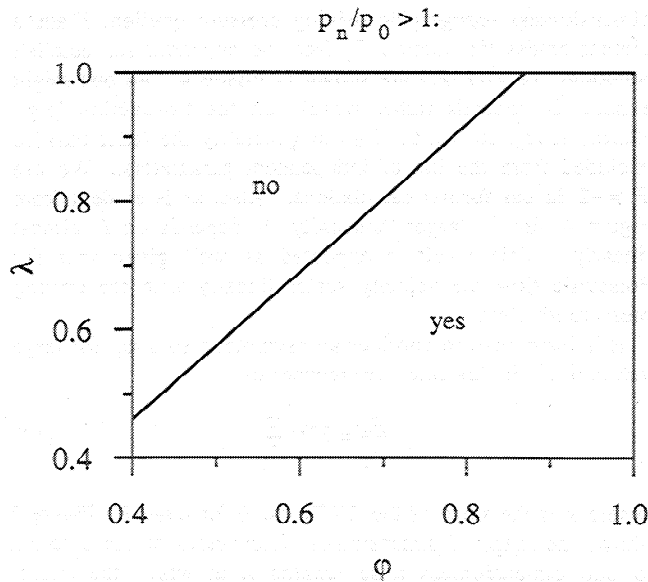
$p_n/p_0 > 1$:

Figure 5. Range of parameters φ and λ illustrating when the pressure at the base of the 2-D dike nose exceeds the pressure in the dike tail.

where $\omega(0)$ is a dimensionless thickness at the base of the nose that depends upon the dimensionless driving pressure gradient Γ and is found as a part of the solution to the problem discussed in the appendix. Combining (15), (17), and (18), we obtain $p_n/p_0 = \omega(0)k^{-1/2}$. Numerical solutions indicate that for $\Gamma > 1$ the values of $\omega(0)$ somewhat exceed 0.9, while k is approximately constant and equals ~0.7 (Figure 4). This shows that in the asymptotic case of large Γ the ratio p_n/p_0 is larger than unity, and thus for sufficiently large slopes the excess magma pressure may increase toward the leading edge of the dike.

The next important step is to identify the critical slope at which p_n/p_0 exceeds unity. Because Γ implicitly depends on p_n/p_0 through (15), one needs to make use of a particular relationship between p_0 and h (i.e., equations (3) or (4)) in order to solve (16). Rewriting (16) and accounting for (3), (4), (15), and (18), we obtain

Density step
$$\left(\frac{p_n}{p_0}\right)^3 = \frac{\pi}{4}\frac{v(\Gamma)}{\omega(0)}\frac{\rho_d}{\Delta\rho}\alpha,$$

$$\Gamma\omega(0) = \frac{\pi}{4}\frac{\rho_d}{\Delta\rho}\frac{p_0}{p_n}\alpha. \qquad (19)$$

Density gradient
$$\left(\frac{p_n}{p_0}\right)^3 = \frac{4}{3}\frac{v(\Gamma)}{\omega(0)}\rho_d\left(\frac{g}{p_0R}\right)^{1/2}\alpha,$$

$$\Gamma\omega(0) = \frac{4}{3}\rho_d\left(\frac{g}{p_0R}\right)^{1/2}\frac{p_0}{p_n}\alpha \qquad (20)$$

(using the appropriate values $\varphi = 1/2$ and $\varphi = 2/3$ in equations (19) and (20), respectively). Equations (19) and (20) were solved iteratively to eliminate the dependence of p_n/p_0 on Γ using tabulated values of U and $\omega(0)$. Results of these calculations are shown in Figure 6. For a dike propagating along a density step, the critical slope at which $p_n/p_0 = 1$ is given by
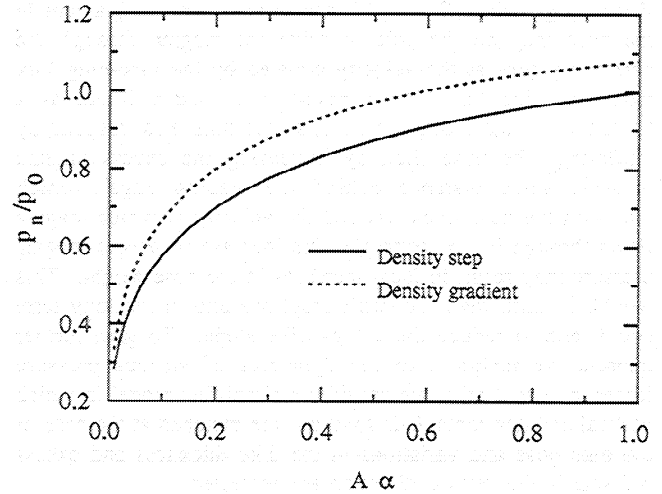

Figure 6. Dependence of the ratio p_n/p_0 on the along-strike slope α. Dimensionless premultiplying factor A equals $\Delta\rho/\rho_d$ in the case of a density step LNB and $(p_0R/\rho_d^2 g)^{1/2}$ in the case of a density gradient LNB. Critical slope α_c corresponds to $p_n/p_0 = 1$.

$$\alpha_c \approx \frac{\Delta\rho}{\rho_d}. \qquad (21a)$$

For a dike propagating along the LNB due to a density gradient, the critical slope is

$$\alpha_c \approx 0.51\left(\frac{p_0R}{\rho_d^2 g}\right)^{1/2}. \qquad (21b)$$

Estimates of the critical slopes for reasonable geophysical parameters are given in section 6. Note that the critical slope for a density step is independent of p_0 (essentially, the excess magma pressure at the source), while for a density gradient it is not.

While these results suggest the possibility of some interesting feedback associated with magma flow in topography-driven dikes, there remain several questions which cannot be addressed by the model considered. First, the model might be misleading because it rather crudely mimics the effects of 3-D elasticity and ignores the essentially 2-D nature of fluid flow within the nose, so that the inferred increases in excess magma pressure within the nose might be an artifact of the simplifying assumptions made. Second, even if dikes do develop increases in the excess pressure within the nose for sufficiently steep slopes, it is unclear whether these increases may translate into increases in dike height, given that the 2-D approximation breaks down within the nose. To verify the possibility of downrift increases in the excess pressure as well as the dike height suggested by our approximate 2-D model, we performed a series of physical experiments and some preliminary steady state 3-D calculations simulating lateral dike propagation in the presence of a topographic driving pressure gradient.

4. Physical Analog Modeling of Downrift Dike Propagation

Most previous experiments simulating dike propagation were carried out by injecting fluid into gelatin [*Fiske and*

Jackson, 1972; *Maaloe*, 1987; *Lister and Kerr*, 1991]. Unfortunately, gelatin experiments offer very little control over the ambient stress field. In addition, while gelatin has a low absolute fracture toughness, the small size of the experimental hydrofractures may result in the main force balance being between the elastic and fracture properties of gelatin, so that the effects of viscous pressure losses in the fluid are small. This is contrary to what is predicted for dikes, and hence similarity between the experiments and large-scale magma fracture at depth does not hold [*Lister and Kerr*, 1991]. To circumvent these problems, we chose a design in which the fluid is forced between two unbonded surfaces held in contact by controlled remote stresses. Thus the flow is resisted by the ambient compressive stress and surface tension only. The experimental apparatus is shown in Figure 7. Three sheets of foam rubber having a total thickness of 0.6 m, length of 1.8 m and breadth of 0.7 m were pressed against a transparent sheet of polycarbonate (Plexiglas) using two PVC panels connected by a "piano" hinge along the flow axis. The angle θ between the panels was regulated by eight screws put on the base PVC sheet on both sides of the hinge. The base PVC sheet was rigidly attached to the Plexiglas lid by a number of steel rods around the perimeter of the apparatus. Thus the ambient stress in the foam rubber was controlled by the Young's modulus of the foam rubber and by the angle θ. Note that if the Plexiglas lid were perfectly rigid and the foam rubber were linearly elastic, such a configuration would approximate a density step LNB with a piecewise linear horizontal stress having a kink at the LNB. In practice, neither of these conditions was strictly satisfied, and the details of the stress distribution at the interface between the foam rubber and the Plexiglas were not known precisely.

The fluid (dyed glycerol) was injected between the transparent plexiglas lid and the foam rubber through a hole in the Plexiglas. To prevent percolation of the fluid into the porous foam rubber, the latter was isolated by a thin latex membrane, so that the fluid was propagating between the Plexiglas and the membrane. In most of the experiments, a constant-pressure boundary condition was enforced at the source by maintaining a constant height in a fluid column above the injection poin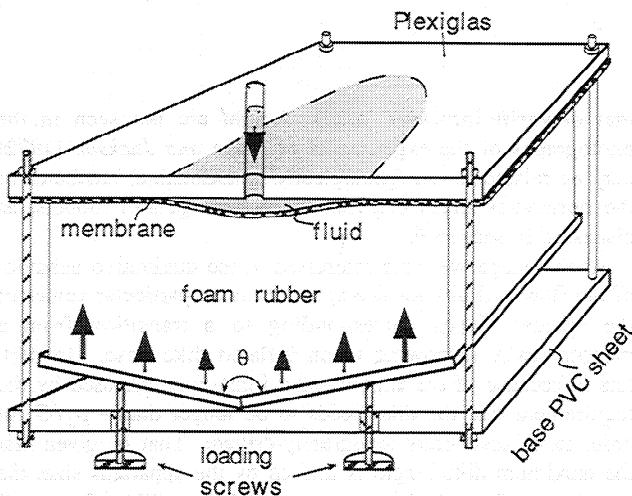t (Figure 7). The topographic driving pressure gradient was introduced by tilting the apparatus in the flow direction at a prescribed angle. The first set of experiments was performed with no tilting, i.e., the driving pressure gradient for flow was provided by the excess source pressure only. Experimentally measured dike shapes normalized by their maximum extent in the vertical and horizontal directions are plotted in Figure 8 against theoretical self-similar dike profiles for the density step and density gradient LNB deduced using the 2-D approximation (e.g., equation (9)). As expected, the theoretical solutions tend to overestimate dike height near the leading edge because of the neglect of 3-D elasticity. Otherwise, the observed dike profiles revealed an overall good fit to the calculated ones. This, together with the good agreement between the experimentally measured and theoretically predicted scaling of the propagation velocity with the inverse square root of time, was taken as indicating that the main balance in the experiment was between elastic and viscous forces, as desired.

In the second set of experiments, we investigated the dynamics of fluid propagation in the presence of large slopes (40-60%). Figure 9 shows a typical flow evolution in time. Upon initiation, the flow is driven mostly by the excess source pressure; asymmetry between the upslope and downslope directions develops when the effect of the topographic driving pressure gradient becomes appreciable. As the fluid propagates farther, a constant height is established in the dike tail. An increase in the height of the dike nose, compared with the height back in the tail, is evident when the dike propagates a distance of about two dike heights (Figure 9a). Variations in the dike height and excess pressure distribution are less apparent beyond this transition; however, one may observe that the color intensity (which is a proxy for dike thickness) along the top and bottom dike edges decreases from the nose to the tail, where it reaches some background value (Figure 9b). This decrease in thickness along the dike perimeter is interpreted as being due to a decrease in the excess pressure: After the passage of the dike nose, fluid is withdrawn from the top and bottom edges, which is reflected in the decreased dike

Figure 7. Schematic view of experimental apparatus.

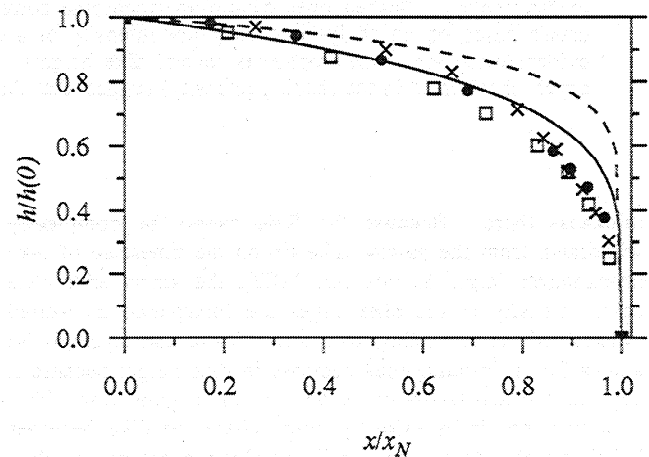**Figure 8.** Comparison of experimental data for flows driven by an excess source pressure to theoretical solutions. Solid and dotted lines correspond to solutions for the density step (equation (9)) and density gradient LNB, respectively. Symbols denote experimental data for different positions of the fluid front (2, 3, and 4 times the dike height for squares, circles, and crosses, respectively).
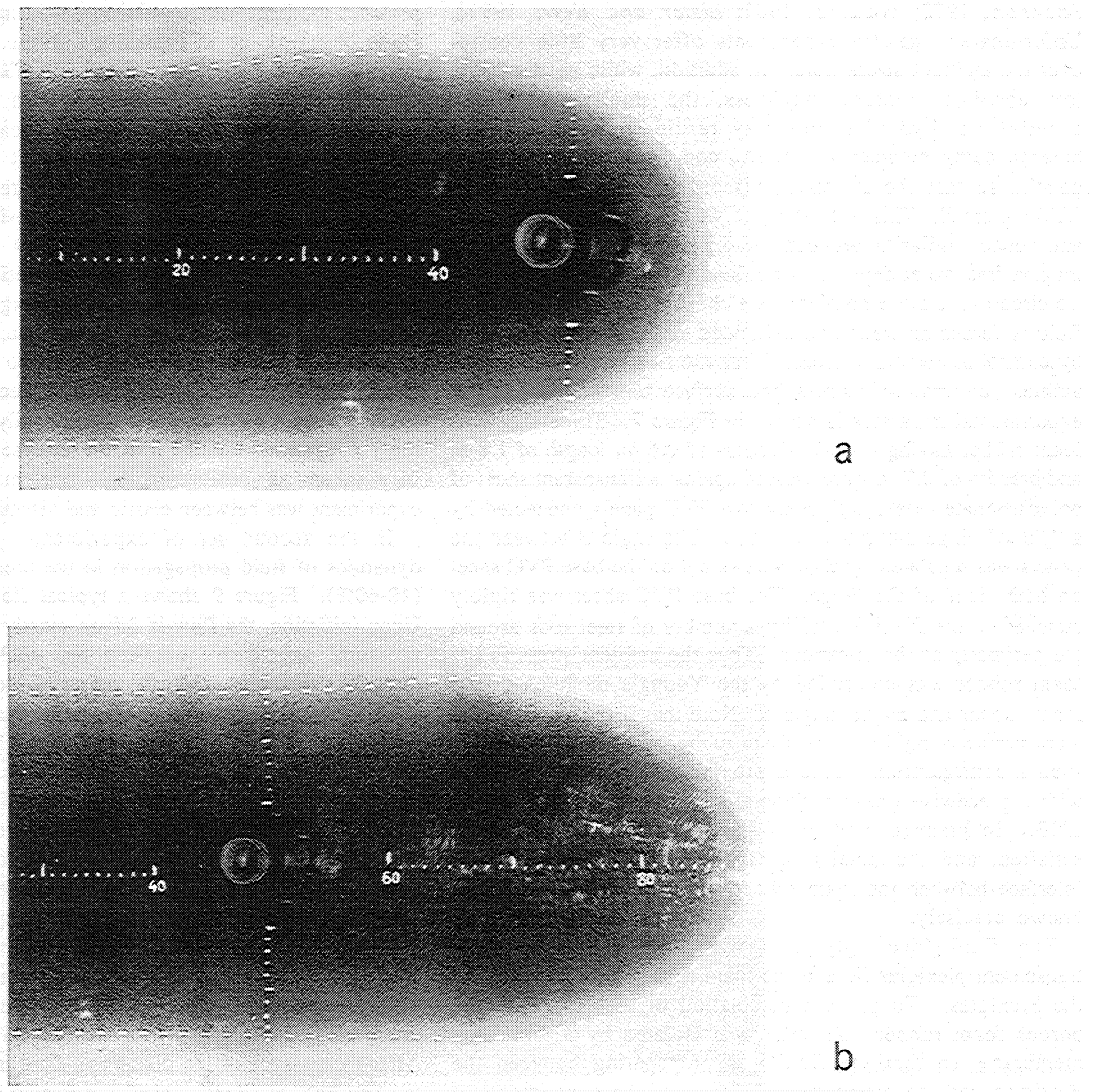
Figure 9. Experimental fluid-driven crack propagating in the presence of a topographic pressure gradient. Scale is in centimeters. Dashed lines denote an isochrome corresponding to the crack thickness at the leading edge; it is drawn based on an analysis of the color intensity of a digitized image. (a) Initial increase in the nose height is evident when the crack propagates several dike heights. (b) Variations in the dike thickness at the top and bottom edges (manifested in the shading intensity) suggest that the dike height is maximum at the base of the nose.

thickness there. Because the fluid cannot be completely withdrawn from the narrow dike tip on the timescale of dike propagation [e.g., *Stevenson*, 1982], the strips with little color intensity at the dike edges are interpreted as wetted "wakes" of the advancing dike nose. (Note that equation (9) allows for an instantaneous decrease in dike height because it neglects the across-stream component of magma flow. This flow becomes infinitesimally slow where the dike becomes infinitesimally thin, which will preclude decreases in dike height but which should not otherwise significantly affect the flow evolution since only small volumes of magma are affected.) It should be mentioned that the dike height is quite constant along the tail in Figure 9b, which indicates that the initial development of the "bulbous" nose seen in Figure 8a was not due to local variations in the ambient stress field. Similar results were obtained for a range of slopes. The fact

that downrift increases in dike height are not seen in the photographs of the experiments of *Fiske and Jackson* [1972] may be related to the (geologically unreasonable) attributes of the horizontal stress distribution in their gelatin models, as discussed in section 6.

At this stage we were interested in the qualitative behavior of the flow and did not attempt to measure particular values of the critical slopes corresponding to a transition from a monotonically narrowing to an inflated dike nose. In part, this is because of the experimental limitations imposed by the requirement that the dike needs to be longer than $\sim p_s/G$ in order to be essentially topography-driven. That is, given that the maximum dike length is limited by the apparatus size, the only way of producing topography-driven dikes for small slopes is by reducing the source pressure p_s. However, observations become more problematic for small p_s because

variations in the ambient stress become nonnegligible (compared with p_s), and decreases in dike width result in the increasing importance of surface tension relative to viscous flow. Also, the dike height (as defined by the boundary between wetted and unwetted regions) was found to be time-dependent even for a constant excess fluid pressure. That is, after rapidly reaching a quasi-constant value for a given pressure at the dike center, the dike height continued to diffusively increase with time, perhaps due to capillary effects. For these reasons, visual identification of increases in dike height may be quite cumbersome, as evidenced by Figure 9b, and become more so as the overall thickness decreases.

5. Hints From Three-Dimensional Simulations

To further support our 2-D numerical and 3-D analogue models, we performed some preliminary steady state calculations for the dike nose using fully coupled 3-D elasticity and 2-D fluid flow. Because of symmetry (we neglect the free surface), we consider only the lower half of the dike, $z \geq 0$ (Figure 2). The computational domain consists of a dike nose having length l, within which the dike height increases monotonically from zero to the constant "tail value," and a portion of the dike tail having length bl, where b is a constant. Note that b should be large enough such that the "upstream" end of the computational domain (at $x_u = x_N - (b+1)l$) resides within the region where plane strain conditions are satisfied in a vertical cross section. We normalize spatial coordinates with respect to the half height of the dike tail $\hat{h} = h(x_u)$, $\zeta = z/\hat{h}$, and $\xi = (x_N - x)/\hat{h}$ as before and introduce the effective dynamic fluid pressure

$$\tilde{p}(\xi, \zeta) = \bar{p}(\xi, \zeta) - (\xi + (b+1)\lambda)\gamma + \zeta \upsilon, \qquad (22)$$

which is defined as the difference between the nondimensional excess magma pressure $\bar{p}(\xi, \zeta) = p(x, z)/p(x_u, 0)$ (first term on the right-hand side) and static contributions from the dimensionless driving pressure gradient γ (second term) and dimensionless vertical gradient in the excess magma pressure υ (third term). For a dike propagating along a density step LNB (the case to which we limit our attention in this section), the static vertical fluid pressure gradient in (22) is $\upsilon = \text{const} = -\pi/2$ (equation (3)). At the upstream end ($\xi = \xi_u = -(b+1)\lambda$), 2-D elasticity and 1-D fluid flow are assumed to hold. This implies a uniform upstream boundary condition for the dynamic pressure

$$\tilde{p}(\xi_u, \zeta) = 1. \qquad (23)$$

The fluid dynamics is governed by the steady state continuity equation

$$\nabla \cdot \left(\bar{w}^3 \nabla \tilde{p} \right) = -\gamma \varpi \frac{\partial \bar{w}}{\partial \xi}, \qquad (24)$$

where $\bar{w}(\xi, \zeta)$ is the dike width normalized by (5) and the product $\gamma \varpi$ represents the nondimensional nose velocity (γ and ϖ are defined in equations (6) and (7)). The dike width $\bar{w}(\xi, \zeta)$ is related to the excess magma pressure $\bar{p}(\xi, \zeta)$ through 3-D elasticity,

$$\bar{w}(\xi, \zeta) = \int_D \Im(\xi, \zeta; X, Z) \bar{p}(X, Z) dX dZ, \qquad (25)$$

where D is the dike area and $\Im$ is an appropriate Green's function. The problem is closed by specifying the initial dike height profile $\hat{h}(\xi)$ (in most calculations chosen based on the

results of the physical modeling) and pressure distribution $\bar{p}(\xi, \zeta)$ and by the requirement of zero flux across the dike perimeter and centerline (i.e., $\hat{h}(\xi)$ and the symmetry axis $\zeta = 0$). The resulting system of equations was solved iteratively for particular values of the of the governing parameter γ (the ratio of the topographic pressure gradient to the vertical gradient in the excess magma pressure). Equation (24) was approximated by a second-order finite difference scheme. After the excess magma pressure was updated from (22) and (24) based on the current dike thickness, the new dike thickness was calculated from (25) using a 3-D boundary element method [Rubin, 1992]. In order to reduce the degree of nonlinearity of the problem, elements of the mesh along the dike perimeter could be removed from the computational grid (i.e., if the pressure was sufficiently low that interpenetration of an element occurred at some iteration step), but no elements could be added. Iterations were continued until the pressures converged with a relative accuracy of 10^{-2} (note that convergence criteria are more stringent for pressures than for thickness because of the averaging effect of the integral operator in equation (25)). Numerical experiments showed that the final pressure and thickness distributions are independent of initial conditions provided that the latter are reasonably smooth. To prevent spurious oscillations along the upper edge of the dike where $\bar{w}$ and $\partial \bar{w}/\partial \zeta$ tend to zero as $\zeta \to 1$, we used values of υ in (22) somewhat larger than $\partial \bar{w}/\partial \zeta$, which effectively resulted in nonzero stress-intensity factors at the dike top and bottom.

Figure 10 shows the results of computations for $\gamma = 0.2$. As can be seen, the nose develops increases in both the excess pressure and dike thickness. Note that while the maximum dike thickness occurs roughly at the junction between the nose and the tail, the maximum in excess magma pressure is shifted toward the leading edge. The same result was also obtained in the 2-D simulations described in section 3. Although the dike height was not allowed to adjust to increases in the fluid pressure, potential variations in dike height can be inferred from the near-tip dike thickness, which is a proxy for the stress intensity factor at the tip [e.g., Lawn and Wilshaw, 1975]. Using this criterion, it is apparent from Figure 10b that there is a tendency for local increases in the dike height just behind the base of the nose. Maxima in both the excess pressure and dike thickness disappear as γ decreases. Unfortunately, the computational task becomes prohibitive for grid sizes less than 0.02 (i.e., for more than ~50 grid points along the dike height) and for $b > 2$ when $\lambda = 2$ (i.e., for a dike tail longer than two full dike heights). For this reason we were not able to observe convergence of our solution with mesh refinements. In the explored range of parameters, calculations show that the magnitude of nose inflation (for fixed values of γ and b) tends to decrease with increasing resolution; however, it increases with increasing values of b. The increase with b is not surprising given that in Figure 10 the driving pressure gradient due to topography is only twice that due to the excess pressure. Note that steady state propagation implies an asymptotic solution for arbitrarily large values of b; consistent with this, in the numerical calculations, $\partial \bar{p}/\partial \xi$ at the upstream end of the dike tail decreases as b increases. However, the precise amplitudes of the increases in excess fluid pressure in the dike nose for supercritical values of γ, and the critical value of γ, remain to be resolved. Another problem that may be addressed in future work is the coupling of the dike height to the excess fluid pressure. This can be done by

introducing a fracture criterion and uniformly enforcing the latter everywhere along the dike edge. The "true" shape of the dike nose may ultimately be obtained from such a simulation.

6. Discussion

Near-tip excess pressure increases in laterally propagating topography-driven dikes are in some ways analogous to those in vertically propagating buoyant dikes [e.g., *Spence and Turcotte*, 1990; *Lister and Kerr*, 1991]. For sufficiently tall dikes driven by magma buoyancy (analogous to sufficiently long dikes driven by a topographic slope), there is a tail of nearly constant thickness where the excess pressure is zero and the flow is driven by $\Delta\rho g$ (analogous to a tail of nearly constant thickness where the excess pressure is constant and the flow is driven by $\rho_d g \alpha$). In both cases an increase in the elastic thickness at some distance behind the leading edge decreases the pressure gradient upstream of that position and increases the local excess pressure; this provides for an increased pressure gradient downstream of that position capable of carrying the flow through the narrowing nose at the velocity dictated by the tail. However, there are some important differences. For buoyancy-driven dikes the tail thickness is controlled by the volume flux from the source and elasticity is unimportant; for topography-driven dikes the tail thickness is controlled by the excess source pressure and elasticity. More fundamentally, for buoyancy-driven dikes the increase in excess pressure stems from the necessity to generate a positive dike thickness; if the pressure gradient increased (and the excess pressure decreased) monotonically from the tail to the tip in order to move the magma through the narrowing nose, the excess pressure would be everywhere negative. For topography-driven dikes the excess pressure in the dike tail is positive, so the increased pressure near the nose comes not from the need for a positive thickness but from the need to compensate for decreases in the nose thickness imposed by 3-D elasticity. Among other things, this difference implies that while all buoyancy-driven dikes possess a nose that is thicker than the tail, whether or not topography-driven dikes do so depends upon the topographic slope.

As indicated by our analysis, the critical along-strike slopes at which increases in the excess magma pressure start to develop near the dike leading edge are governed by the dimensionless group $\Delta\rho/\rho_d$ or $(p_0 R/\rho_d^2 g)^{1/2}$ in the case of the density step and density gradient LNB, respectively (see equations (19)-(21) and Figure 6). For subaerial rift zones, ρ_d essentially equals the magma density (~2600 kg/m³), while for submarine zones ρ_d is given by the density difference between magma and seawater (~1600 kg/m³). Using $\Delta\rho = 200$ kg/m³ as a characteristic density contrast between the magma and host rocks (corresponding, e.g., to rock densities of 2400 and 2800 kg/m³ above and below the LNB, respectively), from (21a) we obtain critical slopes of 8% and 13% for subaerial and
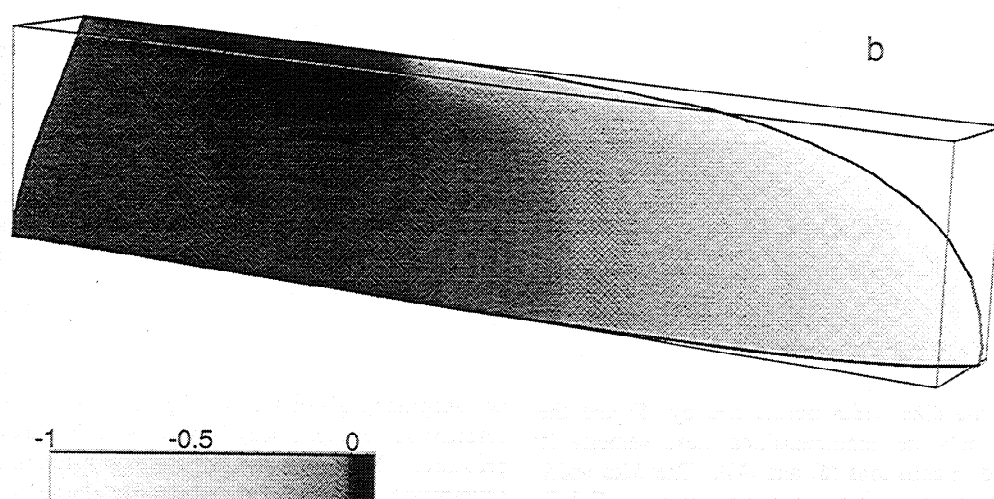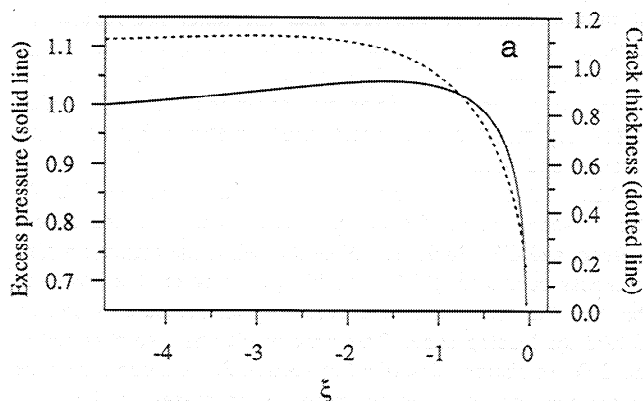

Figure 10. Results of coupled elastic-hydrodynamic 3-D steady state calculations of the dike nose shape for $\gamma = 0.2$. (a) Profiles are of the excess pressure and dike aperture along the dike centerline. (b) Three-dimensional plot of the dike. Shading denotes along-strike variations in the dike thickness with respect to the thickness at the upstream end where 2-D elasticity and 1-D flow are assumed to hold, $\overline{w}(\xi,\zeta)/\overline{w}(\xi_u,\zeta)-1$. Relative increases in the dike thickness are especially pronounced near the dike tip at the base of the nose, which implies local increases in the stress intensity factor and a tendency for increases in the dike height.

submarine rift zones, respectively. Critical slopes resulting from the density gradient LNB may be a factor of 2-3 smaller; using $R = 0.05$ kg/m^4 (corresponding, e.g., to a density increase from 2350 kg/m^3 at the surface to 2850 kg/m^3 at a depth of 10 km), and $p_0 = 2$ MPa (consistent with typical dike heights of several kilometers; see equation (4)), we obtain critical values of 2% for subaerial and 3% for submarine rift zones. The preliminary 3-D calculations suggest that the critical slopes may be lower still. These values may be compared with the observed slopes of basaltic shield volcanoes worldwide [e.g., *Fielder and Wilson*, 1975, Figure 6.2]. In Hawaii, subaerial rift zones are, on average, characterized by along-strike slopes of a few percent [*Holcomb*, 1987]. Mature submarine rifts exhibit remarkably constant slopes of 7-8%, while the southern flanks of Mauna Loa and Loihi seamount have very steep slopes of up to 20% (see Figure 1). Although it might be tempting to interpret these differences in terms of variations in the density structure of these rift zones, it is noteworthy that the two submarine volcanic rift zones characterized by the steepest along-strike slopes also have abnormally steep across-strike slopes [*Fornari*, 1987, Figure 5.4]. Large across-strike slopes result in horizontal compressive stresses that at shallow levels increase more slowly with depth than the vertical stress [*Dieterich*, 1988]. This implies larger values of the effective $\Delta \rho$ or p_0 than would be produced by density contrasts alone, as the effective $\Delta \rho$ or p_0 are determined by the difference between the magma pressure and the dike-perpendicular stress. From (21), these increased values of $\Delta \rho$ or p_0 would indeed give rise to larger critical along-strike slopes.

Because the gelatin models used in the experiments of *Fiske and Jackson* [1972] had very steep across-strike slopes (75%, which is a factor of 4 steeper than typical across-strike slopes in Hawaii), a very large critical along-strike slope in their experiments may be expected. Finite element calculations of *Dieterich* [1988] indicate that the experimental geometry of Fiske and Jackson gives rise to a horizontal stress that is independent of (or even decreases with) depth in the upper part of their gelatin "ridge" [*Dieterich*, 1988, Figure 6]. This implies that the vertical gradient in the excess fluid pressure is essentially given by the hydrostatic pressure gradient in the fluid, in which case (21) gives rise to a critical slope of $O(1)$. Note that because expressions (21) were obtained under the assumption $\alpha \ll 1$, they cannot be used in the limit of steep slopes. Extension of the analysis presented in sections 2 and 3 for an arbitrary slope indicates that the critical along-strike slopes in the experiments of *Fiske and Jackson* [1972] should be of the order of 45° or more, greatly exceeding the slopes they used. This may explain why dikes in their experiments did not exhibit downslope increases in the dike height.

Variations in across-rift topography may also bear on the origins of breaks in the along-strike slopes of volcanic rift zones. For example, our model predicts a break in slope at the passage of a subaerial to a submarine volcanic rift zone due to a step change in differential density ρ_d (see equations (21)); for ρ_d changing from 2600 to 1600 kg/m^3 as the dike propagates from a subaerial to a submarine rift, the expected increase in the critical slope is a factor of 2.6/1.6~1.6. The observed break in slope, for example, from the Kilauea East Rift Zone to the Puna Ridge is about a factor of 3 (from 2.5 to 7-8%), substantially larger than is predicted. This discrepancy could be explained by the fact that the subaerial East Rift Zone of Kilauea is essentially a one-sided ridge buttressed by Mauna

Loa on the north, while its submarine continuation is more symmetric, with well-developed slopes on both sides. The "mass deficiency" produced by the across-strike topography is likely to give rise to a horizontal stress that increases more slowly with depth, which, as discussed above, would increase the critical slopes compared with models in which the LNB was generated by density contrasts alone.

The analysis above indicates that the critical slopes of volcanic rift zones are independent of magma viscosity and the elastic modulii of the host rocks (see equations (21)). These results apparently contradict a well-established relation between magma composition and the morphology of major terrestrial volcanoes (e.g., silicic volcanoes are known to have generally steeper slopes than their mafic counterparts). Note that even though differences in magma viscosity do not affect the overall dynamics of the model presented, they do affect the timescales involved. This is suggestive of the importance of thermal controls on magma emplacement [*Delaney and Pollard*, 1982; *Fialko and Rubin*, 1998]. Thermally limited magma emplacement may be partly responsible for why silicic volcanoes do not develop volcanic rift zones in which magma is transported laterally in dikes. Instead, steep (50% and more) slopes of andesitic stratovolcanoes are believed to be controlled by the angle of repose of the pyroclastic material comprising the bulk of the volcanic edifice [e.g., *Bullard*, 1984].

We point out that the results of both the physical and numerical modeling indicate that potential downrift increases in dike height (and thus the increased tendency for dikes to erupt) may be rather small (of the order of a few percent of the dike height). Under in situ conditions, these effects could be dwarfed by the presence of reasonable along-strike inhomogeneities in the dike-perpendicular stress. If so, the latter might dictate where eruptions occur during individual diking events (even though the long-term eruptive behavior could still be controlled by the mechanism discussed above). However, other physical aspects of lateral dike propagation (omitted from our models) may enhance the tendency for downrift eruptions. First, we did not consider the effect of the free surface, which is expected to become substantial for dikes whose depth is comparable to their height. Elastic solutions for 3-D blade-like cracks demonstrate that the free surface is more effective at increasing the thickness in the dike tail than at the leading edge [*Shah and Kobayashi*, 1973]. Because of the dependence of flow velocity on square of the dike thickness, this would increase the flux within the dike tail more than within the nose, thus increasing the nose pressure necessary to carry away the magma delivered by the tail.

Second, we assumed that the rock fracture resistance is zero. This assumption is justified provided rock fracture energies measured in the lab are applicable to rock failure at depth [e.g., *Lister and Kerr*, 1991]. However, as pointed out by *Rubin* [1993] and *Fialko and Rubin* [1997], field observations of large process zones and dike-induced seismicity, as well as experiments performed under in situ stress conditions, suggest substantially larger fracture energies than those deduced from zero-pressure laboratory tests. If the rock fracture resistance is significant, propagation of the dike nose will be impeded, which implies a stronger tendency for pressure buildup and local increases in the dike height. Note that in the limit of very large rock fracture toughness (such that viscous forces are negligible), the equilibrium dike shape would reflect an essentially hydrostatic increase in the excess magma pressure

from the source to the leading edge. Such "high toughness" behavior was observed in one series of analog experiments in which the rubber membrane adhered to the Plexiglas sheet.

Third, we neglected thermodynamic aspects of magma flow. Effects of temperature-dependent magma rheology on viscous pressure losses in topography-driven dikes are potentially profound. As suggested by *McConnel* [1967] and *Fujii and Uyeda* [1974], basic dikes driven by pressure gradients of $O(10^3)$ Pa/m and having thicknesses greater than ~1 m may experience a "thermal runaway" in which a positive feedback occurs between an increasing magma flux and a decreasing magma viscosity due to shear heating (viscous dissipation). The onset of thermal runaway in topography-driven dikes might result in downrift decreases in the excess magma pressure (and dike cross-sectional area) in order to offset increases in magma flux due to decreasing magma viscosity ("shear thinning"). However, calculations employing realistic magma rheologies and allowing for phase transitions indicate that for reasonable geological parameters thermal runaway is unlikely to occur in dikes that are thinner than ~2.5 m (upublished results by the authors). This condition is satisfied for the majority of dikes in Hawaiian rift zones [*Pollard et al.*, 1983; *Knight and Walker*, 1988], and therefore we conclude that the temperature-dependence of the flow dynamics is likely dominated by conductive cooling.

Magma cooling and freezing are expected to be most pronounced where the dike is thinnest, i.e., at the dike top and bottom and near the dike leading edge. Near the dike leading edge, freezing may affect the overall flow dynamics by reducing the nose thickness and thus slowing down the magma. As illustrated by the 2-D calculations of *Fialko and Rubin* [1998, Figure 11], when the dike is on the verge of thermal arrest, the magma flow is blocked first near the dike tip (even though the chilled margin thickness is minimum there). If blockage is strongly concentrated near the tip, the effects of magma freezing on the excess magma pressure would be analogous to a high fracture toughness, i.e., increases in height may be encouraged toward the leading edge of a dike. Similar effects may be produced by near-tip increases in magma viscosity, for example, due to cooling and/or volatile exolution into the tip cavity (a low-pressure region ahead of the moving magma front). In order to quantify these effects, however, full interaction between magma freezing and flow dynamics must be considered. Finally, we would like to emphasize the possibility that magma freezing may in fact govern temporal and spatial variations in the horizontal stresses along the rift. This stems from the fact that most rift zones have horizontal extents that are of the order of the thermal arrest distances of laterally propagating dikes [*Fialko and Rubin*, 1998]. Following freezing near the leading edge of a topography-driven dike, continued flow behind the leading edge may produce a nearly hydrostatic increase in the horizontal stress that would be "frozen in" upon complete solidification. The next dike might respond to this along-strike increase in the dike-normal stress by erupting uprift of the termination of the previous dike. This cycle may be continued uprift until compressive horizontal stresses along the rift zone are relieved by some tectonic mechanism [e.g., *Dieterich*, 1988]. In this case, the positioning of the eruption sites, and in the long term the along-rift topography, would be controlled by some complex interaction between the fluid dynamics of dike propagation, magma freezing, and variations in the dike-perpendicular stress that have some "memory" of the previous volcanic episodes.

7. Conclusions

We considered the dynamics of viscous pressure losses in lateral dikes propagating in the presence of small along-strike topographic slopes. Dikes that are shorter than the transitional length of $O(p_s/G)$, where p_s is the excess magma pressure at the source and G is the driving pressure gradient due to topography, are driven mostly by the excess pressure and are tallest near the source. If the source pressure is sufficient for magma to reach the surface, such dikes are most likely to erupt near the source. Longer (essentially topography-driven) dikes may erupt anywhere along their length for small enough slopes. For sufficiently large slopes, a topography-driven dike may develop an increase in the excess magma pressure near the leading edge ("nose"), as a result of the 3-D nature of the elastic deformations. This, in principle, may result in a local increase in dike height, thus favoring downrift eruptions. Such behavior implies the existence of a critical along-rift slope at which dikes propagate in equilibrium with the slope (i.e., maintaining it in the long term by preferentially choosing where to erupt). We presented 2-D and preliminary 3-D solutions for the coupled fluid-mechanical/elastic problem in which the dike nose is assumed to propagate at steady state at the velocity dictated by the flux from the dike tail. We also performed physical analog experiments simulating lateral dike propagation along the level of neutral buoyancy in the presence of along-strike topography. Our results have confirmed the possibility of increases in both excess magma pressure and dike height for supercritical slopes. Our estimated values of critical slopes are in general agreement with observations of volcanic rift zones in Hawaii. Quantitative application of these results to specific geological examples is complicated by processes that we have not explicitly considered (e.g., lateral variations of the horizontal tectonic stress and magma freezing). Nonetheless, the observation that lava flows in Hawaii flow essentially perpendicular to the rift zones indicates that the dynamics of lava freezing cannot explain the observed constancy of along-rift slopes. Our results suggest that these slopes could result from viscous pressure losses within laterally propagating dikes.

Appendix

Consider a steadily propagating two-dimensional elastic crack having length l (of the order of the half height of the dike "tail;" see Figure 2) filled by a fluid that enters the crack under fixed excess pressure p_n. Flow in the crack is driven by the viscous pressure drop in the fluid and by a constant external driving pressure gradient G (e.g., due to gravity). Let x be the along-crack coordinate with the origin at the crack base. The crack profile $w(x)$ is governed by the distribution of excess pressure $p(x)$ within the crack,

$$w(x) = \frac{1}{\pi M} \int_0^l \ln \left| \frac{\left(l^2-x^2\right)^{1/2} - \left(l^2-s^2\right)^{1/2}}{\left(l^2-x^2\right)^{1/2} + \left(l^2-s^2\right)^{1/2}} \right| p(s)ds , \qquad (A1)$$

where M is elastic stiffness (see text). Strictly speaking, (A1) is applicable to the symmetrically loaded 2-D crack in an infinite body (with symmetry about $x = 0$). The pressure distribution $p(x)$ inside the crack is determined by viscous pressure losses in the fluid and by the exolution of volatiles in the tip cavity (the region behind the crack tip $l_f < x < l$ where the fluid does not penetrate because of the large viscous

pressure drop along the narrowing crack aperture, l_f being the position of the fluid front within the crack). The cross-sectionally averaged equation of mass continuity gives rise to the following expression for the driving pressure gradient in the fluid:

$$\frac{dp}{dx} - G = -\frac{3\eta u_{nose}}{w^2(x)}, \tag{A2}$$

where η is the fluid viscosity and u_{nose} is the nose velocity. Equation (A2) states that the average fluid velocity is constant and equals u_{nose} in every cross section along the crack, consistent with the assumption of steady state propagation. Assuming that the intrinsic rock strength is negligible [e.g., Lister and Kerr, 1991], equilibrium conditions provide an additional constraint on the pressure distribution within the crack,

$$\int_0^l \frac{p(x)dx}{\left(l^2-x^2\right)^{1/2}} = 0. \tag{A3}$$

Natural boundary conditions at the nose entrance and at the magma front are

$$p(x) = p_n \text{ at } x = 0 \quad p(x) = -p_t \text{ for } l_f \leq x < l, \tag{A4}$$

where $-p_t$ is the tip suction [see, e.g., Rubin, 1993].

System (A1)-(A4) was nondimensionalized using l as the length scale $\hat{x}$, p_n as the pressure scale $\hat{p}$, lp_n/M as the width scale $\hat{w}$, and $lp_n^3/3\eta M^2$ as the velocity scale $\hat{u}$,

$$\omega(\chi) = \frac{1}{\pi}\int_0^1 \ln\left|\frac{\left(1-\chi^2\right)^{1/2}-\left(1-s^2\right)^{1/2}}{\left(1-\chi^2\right)^{1/2}+\left(1-s^2\right)^{1/2}}\right| P(s)ds, \tag{A5}$$

$$\frac{dP}{d\chi} - \Gamma = \frac{U}{\omega^2(\chi)}, \quad \Gamma = \frac{Gl}{p_n} \tag{A6}$$

$$\int_0^1 \frac{P(\chi)d\chi}{\left(1-\chi^2\right)^{1/2}} = 0, \tag{A7}$$

$$P(0)=1; \quad P(\chi)=-P_t \text{ for } \chi_f \leq \chi < 1, \tag{A8}$$

where $\chi = x/\hat{x}$, $\omega = w/\hat{w}$ is the nondimensional elastic crack thickness, $P = p/\hat{p}$ is the nondimensional fluid pressure, $U = u_{nose}/\hat{u}$ is the nondimensional nose velocity, and χ_f is the dimensionless position of the fluid front ($0<\chi_f<1$). System (A5)-(A8) was solved simultaneously for the pressure distribution $P(\chi)$, crack thickness $\omega(\chi)$, velocity U, and position of the fluid front χ_f using iterative techniques for a range of values of Γ. The fluid pressure distribution was approximated by 200 segments along the crack in which the pressure was assumed to vary piecewise linearly. The dependence of the nondimensional crack velocity U on the dimensionless driving pressure gradient Γ and tip suction P_t is shown in Figure 4 in the main text.

Notation

D	dike area in steady state 3-D simulations (equation (25)) (m²).
G	driving pressure gradient due to topography (equation (1)) (Pa/m).
M	host rock elastic stiffness, $M = \mu/(1-\nu)$ (Pa).
P	nondimensional excess fluid pressure.
P_t	nondimensional excess fluid pressure in tip cavity.
R	host rock density gradient (kg/m⁴).
W	nondimensional dike thickness in vertical cross section.
V	dike volume (m³).
U	nondimensional nose velocity.
X	dummy integration variable (equation (25)).
Z	dummy integration variable (equation (25)).
a	exponent specifying dependence of dike volume V on time t, $V \sim t^a$, in model of Lister [1990].
b	nondimensional length of dike tail (in units of dike nose length l) in 3-D simulations.
g	gravitational acceleration (m/s²).
h	dike half height (m).
$\hat{h}$	dike height scale (equation (8)) (m).
$\overline{h}$	nondimensional dike half height.
h_s	dike half height at the source ($x=0$) (m).
k	asymptotic value of $\partial U/\partial \Gamma$ for $\Gamma > 1$ (Figure 4).
l	dike nose length (Figure 2) (m).
l_f	position of magma front within dike nose (m).
p	excess magma pressure (Pa).
$\hat{p}$	excess magma pressure scale (Pa).
$\overline{p}$	nondimensional excess magma pressure (equation (22)).
$\tilde{p}$	nondimensional dynamic magma pressure (equation (22)).
p_s	excess magma pressure at the source ($x=0$) (Pa).
p_n	excess magma pressure at the base of dike nose (Pa).
p_t	excess fluid pressure in tip cavity (Pa).
p_0	excess magma pressure in dike tail at LNB (equations (3) and (4)) (Pa).
s	dummy integration variable (equation (A1)).
t	time (s).
$\hat{t}$	time scale (equation (8)) (s).
$\overline{t}$	nondimensional time.
u_{nose}	velocity of steady-state 2-D dike nose (equation (12)) (m/s).
u_{tail}	average magma velocity in 2-D dike tail (equation (13)) (m/s).
$\hat{u}$	magma velocity scale (m/s).
w	dike half width (m).
$\hat{w}$	dike width scale (m).
$\overline{w}$	nondimensional dike width in 3-D simulations.
w_n	dike half width at the base of dike nose (equation (18)) (m).
w_0	dike half width at LNB (equation (5)) (m).
x	along-strike coordinate (m).
$\hat{x}$	along-strike coordinate scale (m).
$\overline{x}$	nondimensional along-strike coordinate.
x_u	position of upstream end of computational domain in 3-D simulations (m).
x_N	dike length (m).
$\overline{x}_N$	nondimensional dike length.
z	vertical (with respect to LNB) coordinate (see Figure 2) (m).
$\overline{z}$	nondimensional vertical coordinate.
Γ	ratio of driving pressure gradients due to topography and excess magma pressure.
α	along-strike topographic slope (radian).
χ	nondimensional along-strike coordinate in 2-D dike nose.
χ_f	position of fluid front in 2-D dike nose.
φ	nondimensional dike thickness at LNB (equation (5)).
η	dynamic magma viscosity (Pa s).

γ	ratio of driving pressure gradient due to topography to vertical gradient in excess magma pressure.
λ	nondimensional dike nose length (equation (15)).
μ	host rock shear modulus (Pa).
ν	host rock Poisson's ratio.
ρ_d	density difference between magma and air (for subaerial rift zones) or seawater (for submarine rift zones) (kg/m^3).
ρ_m	magma density (kg/m^3).
ρ_0	host rock density at LNB due to density gradient (kg/m^3).
$\Delta\rho$	density contrast between magma and host rocks at LNB due to density step (kg/m^3).
υ	nondimensional vertical gradient in excess magma pressure in dike tail (for density step LNB).
ϖ	nondimensional average magma velocity (equation (7)).
ω	nondimensional half width of 2-D dike nose.
ξ	nondimensional along-strike coordinate in reference frame of moving magma front, $\xi = \bar{x} - \bar{x}_N(\bar{t})$.
ξ_u	nondimensional position of upstream end of computational domain in 3-D steady-state simulations, $\xi_u = -(b+1)\lambda$.
ζ	nondimensional vertical coordinate in 3-D simulations.
$\mathfrak{I}$	Green's function (equation (25)) (s^2/kg).

References

Bullard, F.M., *Volcanoes of the Earth*, 2nd ed., 629 pp., Univ. of Texas Press, Austin, 1984.

Delaney, P.T., and D.D. Pollard, Solidification of basaltic magma during flow in dike, *Am. J. Sci., 282*, 856-885, 1982.

Dieterich, J.H., Growth and persistence of Hawaiian volcanic rift zones, *J. Geophys. Res., 93*, 4258-4270, 1988.

Fialko, Y.A., and A.M. Rubin, Numerical simulation of high pressure rock tensile fracture experiments: Evidence of an increase in fracture energy with pressure?, *J. Geophys. Res., 102*, 5231-5242, 1997.

Fialko, Y.A., and A.M. Rubin, Thermodynamics of lateral dike propagation: Implications for crustal accretion at slow spreading mid-ocean ridges, *J. Geophys. Res., 103*, 2501-2514, 1998.

Fielder, G., and L. Wilson (Eds.), *Volcanoes of the Earth, Moon and Mars*, 126 pp., St. Martin's Press, New York, 1975.

Fiske, R.S., and E.D. Jackson, Orientation and growth of Hawaiian volcanic rifts: The effect of regional structure and gravitational stresses, *Proc. R. Soc. London, Ser. A, 329*, 299-326, 1972.

Fornari, D.J., The geomorphic and structural development of Hawaiian submarine rift zones, in *Volcanism in Hawaii*, edited by R.W. Decker, T.L. Wright, and P.H. Stauffer, pp. 125-132, *U.S. Geol. Surv. Prof. Pap. 1350*, 1987.

Fujii, N., and S. Uyeda, Thermal instabilities during flow of magma in volcanic conduits, *J. Geophys. Res., 79*, 3367-3369, 1974.

Holcomb. R.T., Eruptive history and long-term behavior of Kilauea volcano, in *Volcanism in Hawaii*, edited by R.W. Decker, T.L. Wright, and P.H. Stauffer, pp. 261-350, *U.S. Geol. Surv. Prof. Pap. 1350*, 1987.

Khazan, Y.M., and Y.A. Fialko, Fracture criteria at the tip of fluid-driven cracks in the Earth, *Geophys. Res. Lett., 22*, 2541-2544, 1995.

Knight, M.D., and G.P.L. Walker, Magma flow directions in dikes of the Koolau complex, Oahu, determined from magnetic fabric studies, *J. Geophys. Res., 93*, 4301-4319, 1988.

Lawn, B.R., and T.R. Wilshaw, *Fracture of Brittle Solids*, 204 pp., Cambridge Univ. Press, New York, 1975.

Lister, J.R., Buoyancy-driven fluid fracture: Similarity solutions for the horizontal and vertical propagation of fluid-filled cracks, *J. Fluid Mech., 217*, 213-239, 1990.

Lister, J.R., and R.C. Kerr, Fluid-mechanical models of crack propagation and their application to magma transport in dykes, *J. Geophys. Res, 96*, 10,049-10,077, 1991.

Maaloe, S., The generation and shape of feeder dykes from mantle sources, *Contrib. Mineral. Petrol., 96*, 47-55, 1987.

MacDonald, G.A., A.T. Abbot, and F.L. Peterson, *Volcanoes in the Sea: The Geology of Hawaii*, 2nd ed., 517 pp., Univ. of Hawaii Press, Honolulu, 1983.

Mark, R.K., and J.G. Moore, Slopes of the Hawaiian Ridge, in *Volcanism in Hawaii*, edited by R.W. Decker, T.L. Wright, and P.H. Stauffer, pp. 101-107, *U.S. Geol. Surv. Prof. Pap. 1350*, 1987.

McConnel, R.K., Dike propagation, in *Economic Geology in Massachusetts*, edited by O.C. Farquhar, pp. 97-104, Univ. of Mass. Grad. Sch., Amherst, 1967.

Pollard, D.D., P.T. Delaney, W.A. Duffield, E.T. Endo, and A.T. Okamura, Surface deformation in volcanic rift zones, *Tectonophysics, 94*, 541-584, 1983.

Rubin, A.M., Dike-induced faulting and graben subsidence in volcanic rift zones, *J. Geophys. Res., 97*, 1839-1858, 1992.

Rubin, A.M., Tensile fracture of rock at high confining pressure: Implications for dike propagation, *J. Geophys. Res., 98*, 15,919-15,935, 1993.

Rubin, A.M., and D.D. Pollard, Origins of blade-like dikes in volcanic rift zones, in *Volcanism in Hawaii*, edited by R.W. Decker, T.L. Wright, and P.H. Stauffer, pp. 1449-1470, *U.S. Geol. Surv. Prof. Pap. 1350*, 1987.

Ryan, M.P., Neutral buoyancy and the mechanical evolution of magmatic systems, in *Magmatic Processes: Physicochemical Principles*, edited by B.O. Mysen, pp. 259-288, Geochem. Soc., University Park, Pa, 1987.

Shah, R.C., and A.S. Kobayashi, Stress intensity factors for an elliptical crack approaching the surface of a semi-infinite solid, *Int. J. Fract., 9*, 133-146, 1973.

Spence, D.A., and D.L. Turcotte, Buoyancy-driven magma fracture: A mechanism for ascent through the lithosphere and the emplacement of diamonds, *J. Geophys. Res., 95*, 5133-5139, 1990.

Stevenson, D.J., Migration of fluid-filled cracks: Applications to terrestrial and icy bodies, *Lunar Planet. Sci. Conf., 13th*, 768-769, 1982.

Y.A. Fialko, Seismo Lab 252-21, California Institute of Technology, Pasadena, CA 91125. (email: fialko@gps.caltech.edu)

A.M. Rubin, Department of Geosciences, Princeton University, Princeton, NJ 08544. (e-mail: allan@geo.princeton.edu).